Journal of Oceanography, Vol. 54, pp. 273 to 284. 1998

Temporal and Spatial Variabilities of Japan Sea Surface Temperature and Atmospheric Forcings

PETER C. CHU[1], YUCHUN CHEN[2] and SHIHUA LU[2]

[1]*Naval Postgraduate School, Monterey, CA 93943, U.S.A.*
[2]*Institute of Plateau Atmospheric Physics, Academia Sinica, Lanzhou, China*

(Received 13 May 1997; in revised form 6 March 1998; accepted 21 March 1998)

In this study, we used the National Centers for Environmental Prediction monthly sea surface temperature (SST) and surface air temperature (SAT) data during 1982–1994 and the National Center for Atmospheric Research surface wind stress curl data during 1982–1989 to investigate the Japan Sea SST temporal and spatial variabilities and their relations to atmospheric forcing. First, we found an asymmetry in the correlation coefficients between SST and wind stress curl, which implies that the SST variability at the scales of the order of one month is largely due to atmospheric forcing. Second, we performed three analyses on the data fields: annual mean, composite analysis to obtain the monthly anomaly relative to the annual mean, and empirical orthogonal function (EOF) analysis on the residue data relative to the summation of the annual mean and the monthly anomaly. The first EOF mode of SST accounts for 59.9% of the variance and represents the Subpolar Front. The temporal variation of the first EOF mode implies that the deep Japan Sea could be cooler in cold seasons (November–April) of 1984–1987. Third, we computed cross-correlation coefficients among various principal components and found that the atmospheric warming/cooling is the key factor causing intra-seasonal and interannual SST variabilities.

Keywords:
· Sea surface temperature,
· temporal and spatial variability,
· composite analysis,
· empirical orthogonal functions,
· surface air temperature,
· wind stress curl.

1. Introduction

The Japan Sea, known as the East Sea in Korea, has a steep bottom topography (Fig. 1) that makes it a unique semi-enclosed ocean basin overlaid by a pronounced monsoon surface wind. The Japan/East Sea (hereafter JES) covers an area of 10^6 km^2, has a maximum depth in excess of 3,700 m, and is isolated from open oceans except for small (narrow and shallow) straits which connects the JES to the Pacific Ocean. The warm Tsushima Current, dominating the surface layer, flows in from the Tsushima Strait and carries warm water from the south up to 40°N where a polar front forms (Seung and Yoon, 1995). Most of the nearly homogeneous water in the deep part of the basin is called the Japan Sea Proper Water (Moriyasu, 1972) and is of low temperature and low salinity. Above the Proper Water, warm and saline water which enters through the Tsushima Strait flows northeastward and flows out through the Tsugaru and Soya Strait.

The seasonal variability of the JES sea surface temperature (SST) has been studied by many investigators (e.g., Gong, 1968; Kano, 1980; Isoda *et al*. 1991; Isoda and Saitoh, 1993; Isoda, 1994; Maizuru Mar. Observ., 1997) using limited data sets. For example, based on the satellite infrared (IR) images in the western part of the JES and the routine hydrographic survey by the Korea Fisheries Research and Development Agency in 1987, Isoda and Saitoh (1993) found the SST patterns in winter and spring which are characterized as follows. A small meander of a thermal front was first originated from the Tsushima Strait near the Korean coast and gradually grew into an isolated warm eddy with a horizontal scale of 100 km. The warm eddy intruded slowly northward from spring to summer.

The motivation of this study is to investigate the JES surface thermal variability especially the non-seasonal variability, and the response of JES SST to atmospheric forcing. We used the National Centers for Environmental Prediction (NCEP) monthly SST and surface air temperature (SAT) on $1° \times 1°$ grid for the period 1981–94 (Reynolds, 1988; Reynolds and Marsico, 1993; Reynolds and Smith, 1994) and the National Center for Atmospheric Research (NCAR) surface wind stress curl (Trenberth, *et al*., 1989) on $2.5° \times 2.5°$ grid for the period 1982–1989 to study these problems.

JES experiences two monsoons, winter and summer, every year. During the winter monsoon season, a cold northwest wind blows over the JES (Fig. 2(a)) as a result of the Siberian High Pressure System located over the East Asian continent. Radiative cooling and persistent cold air advection maintain cold air over the JES. The northwest-southeast oriented Jet Stream is positioned at the JES. Such

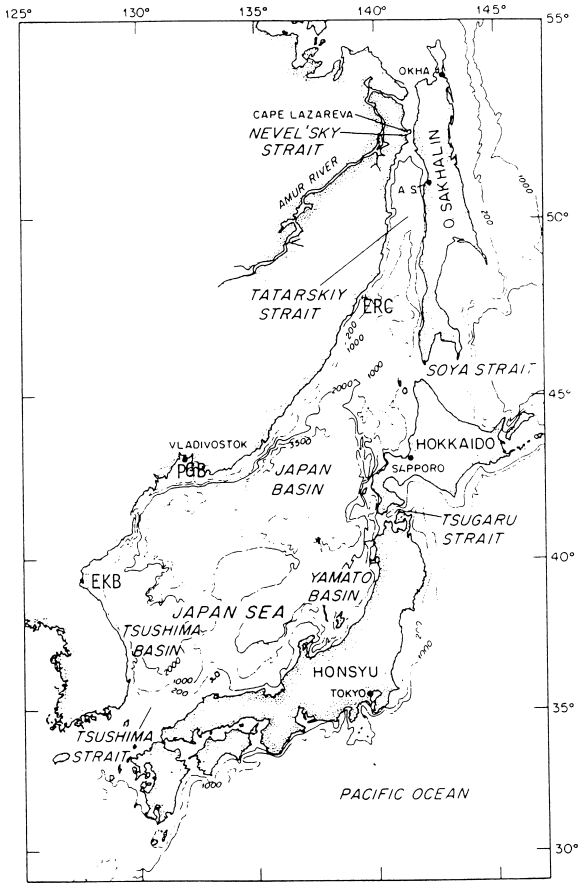

Fig. 1. Geography and isobaths showing the JES bottom topography (from Martin *et al*., 1992) (EKB: East Korea Bay, ERC: East Russian Coast, PGB: Peter the Great Bay).

a typical winter monsoon pattern lasts nearly six months (November to April). During the summer monsoon, a warm and weaker southeast wind blows over the JES (Fig. 2(b)). Such a typical summer monsoon pattern lasts nearly four months (mid-May to mid-September). The NCAR monthly-mean wind field over the JES used in this study is quite similar to the data set produced by Na *et al*. (1992).

2. Annual Mean Fields

We now examine the data to see if the seasonal signal is evident in SST and surface wind stress curl ζ. For convenience, we use $\psi(x_i, y_j, \tau_k, t_l)$ to represent both SST and ζ, where (x_i, y_j) is the horizontal grids, τ_k is the time sequence in years, and $t_l = 1, 2, ..., 12$, the monthly sequence within a year. Before investigating the monthly variation of SST, we define the following two temporal averages:

$$\overline{\psi}\left(x_i, y_j, t_l\right) \equiv \frac{1}{\Delta\tau}\sum_{\tau_k}\psi\left(x_i, y_j, \tau_k, t_l\right)$$

which is the long-term mean value for the month t_l, and

$$\overline{\overline{\psi}}\left(x_i, y_j\right) \equiv \frac{1}{12}\sum_{l=1}^{12}\overline{\psi}\left(x_i, y_j, t_l\right) \qquad (1)$$

which is the climatological annual mean. Here $\Delta\tau = 13$ years for SST and SAT, and $\Delta\tau = 8$ years for ζ.

The annual mean (1982–89) ζ field over the JES (Fig. 3) shows a dipole pattern: cyclonic curls over the Japan

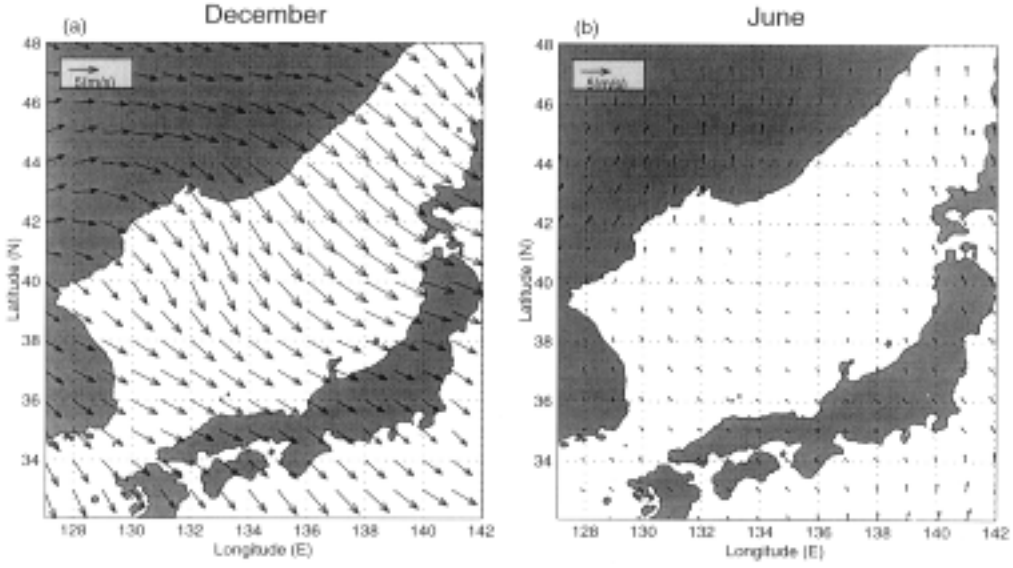

Fig. 2. Mean surface wind vectors in the JES for (a) December, and (b) June (computed from Trenberth, 1989).

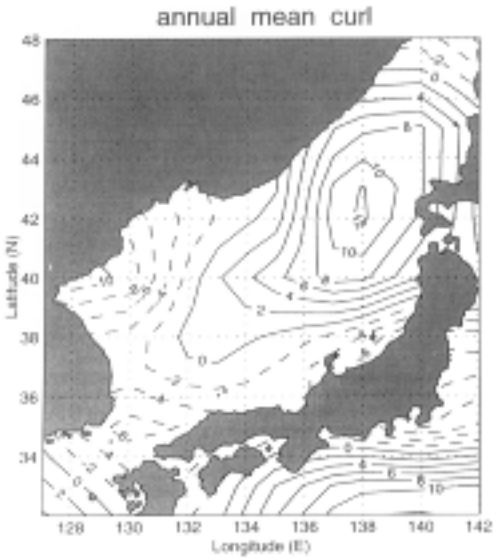

Fig. 3

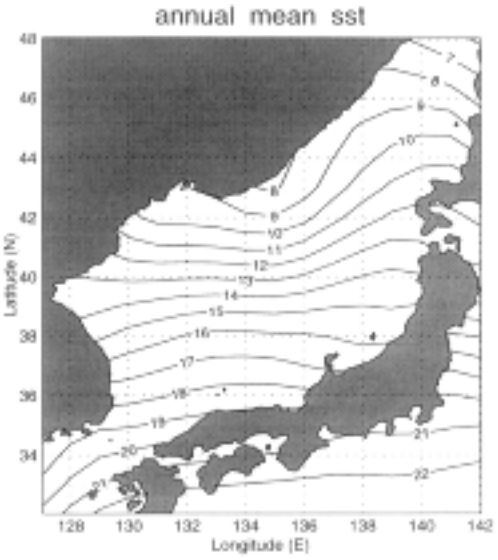

Fig. 4

Fig. 3. The climatological annual mean of the wind stress curl field during 1982–1989. The unit is 10^{-8} N/m^3.
Fig. 4. The climatological annual mean of the SST field during 1982–1994. The unit is °C.

Basin (JB) and anticyclonic curls over the East Korea Bay (EKB). This coincides with the prevailing northwest winds over the central JES. This pattern generally agrees with the surface wind stress curl pattern obtained by Na *et al*. (1992) except in the EKB where a cyclonic curl was identified here.

The annual mean (1982–94) SST field of the JES (Fig. 4) shows a pattern of near-zonal oriented isotherms with a positive temperature gradient towards the southwest near the Tsushima Strait. The annual mean SST decreases from 20°C in the Tsushima Strait to 7°C near the north boundary of JES.

3. Seasonal Variation

The long-term monthly mean values relative to the annual mean,

$$\tilde{\psi}(x_i, y_j, t_l) = \overline{\psi}(x_i, y_j, t_l) - \overline{\overline{\psi}}(x_i, y_j) \qquad (2)$$

represents the composite features of the monthly mean variations of SST, SAT, and wind stress curl.

3.1 Wind stress curl

Seasonal variations of wind stress curl anomaly field are shown in Fig. 5. Basically, the winter anomaly pattern (Fig. 5(a)) is the annual mean pattern (ignoring the amplitude), and the summer anomaly pattern (Fig. 5(c)) is the same pattern with opposite sign. Therefore, the seasonal cycle of the wind stress curl can be understood that the wind stress curl field has a stable (western anticyclonic and eastern cyclonic) pattern, which is strengthened in winter and weakened in summer. The annual mean (Fig. 3) is the middle of these two levels. Similar features of seasonal variation have been pointed out by Na *et al*. (1992).

3.2 SST

Seasonal variations of SST anomaly field are shown in Fig. 6. The JES is found with evident seasonal SST anomalies (Fig. 6): a cold anomaly during the winter (December–February) and a warm anomaly during summer (June–September). These two typical SST anomaly patterns are opposite to each other.

The typical winter anomaly (December to February) $\tilde{T}$ pattern is featured by (a) all negative values, (b) northeast-to-southwest oriented isotherms ($\tilde{T}$ increasing towards southeast), and (c) a cold center located near the PGB. The PGB cold center has the minimum $\tilde{T} \approx -8.4$°C in February (Fig. 6(a)).

The spring (March to May) pattern starts from the weakening of the cold center and occurrence of two weak warm centers: one occurring in early spring near the south Tatarskiy Strait and the other appearing in late spring (Fig. 6(b)) in the EKB. The northward expansion of the EKB warm center leads to the generation of an evident warm center at the PGB, and the summer begins.

The summer (June to September) pattern is opposite to the winter pattern. The typical summer $\tilde{T}$ pattern is featured by (a) all positive values, (b) northeast-to-southwest oriented isotherms ($\tilde{T}$ decreasing towards southeast), and (c) a warm center located near the PGB. The PGB warm center has the

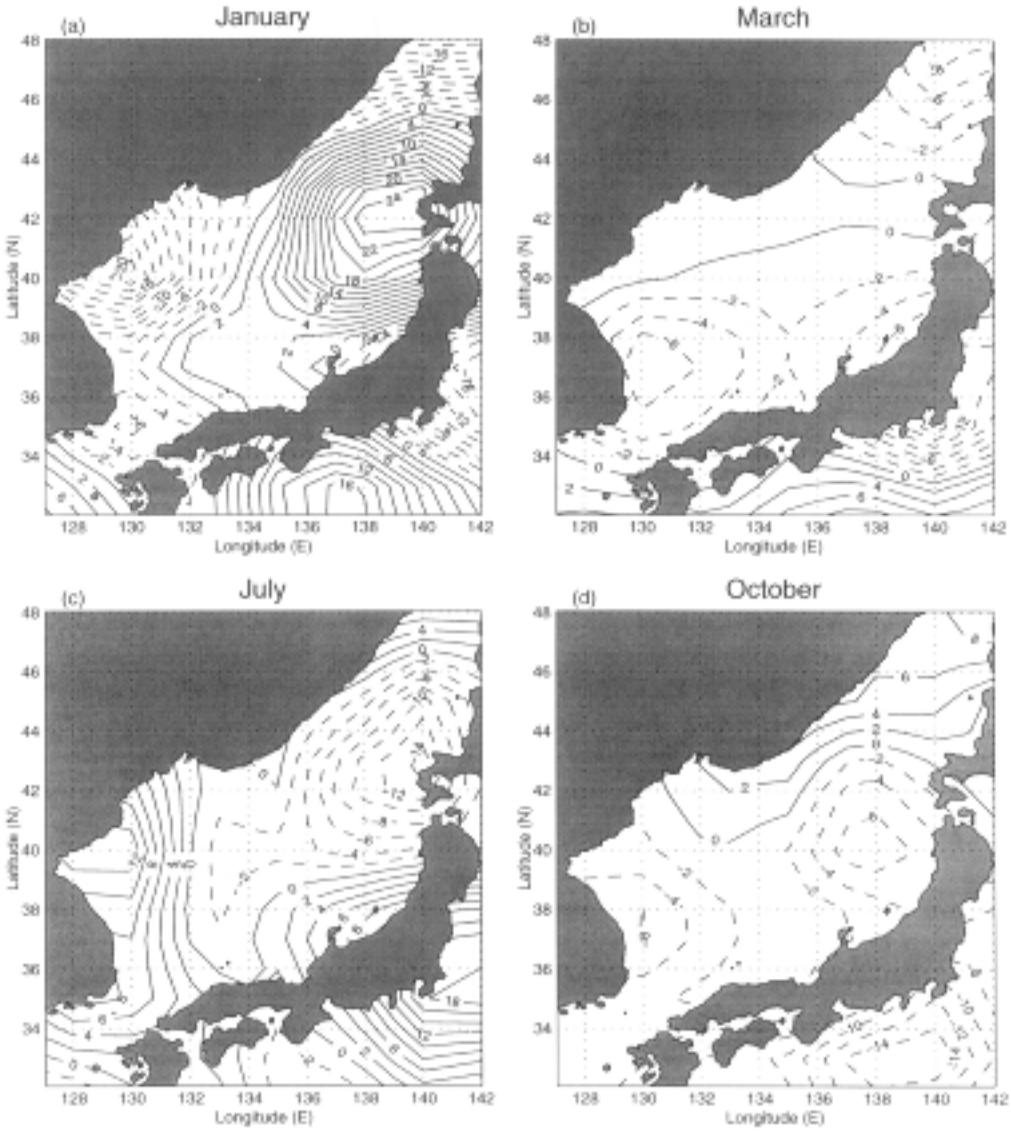

Fig. 5. Monthly surface wind stress curl anomalies relative to the climatological annual mean from the NCAR data set. The unit is 10^{-8} N/m^3.

maximum $\tilde{T} \approx 11.2$°C in August (Fig. 6(c)).

The fall (October to November) pattern features the occurrence of a weak cold center in October (Fig. 6(d)) near the ERC region. The southward expansion of this cold center along the Russian Coast leads to the formation of an evident cold center at the PGB ($\tilde{T} \approx -5.2$°C in December), and the winter starts.

3.3 Cross-correlation coefficient between ζ and T

We interpolated the wind stress curl (ζ) data (2.5° × 2.5°) into the SST grid (1° × 1°), and chose the common period 1982–89 (eight years) for the cross-correlation analysis. Cross-correlation coefficient (CCC) between ζ and T is computed at each grid point by

$$R_{\zeta,T}^{(\tau)}(x,y) = \frac{(t_N - 1)}{(t_N - |\tau|)} \cdot \frac{\sum_t \left\{\left[\zeta(x,y,t) - \overline{\overline{\zeta}}(x,y)\right]\left[T(x,y,t+\tau) - \overline{\overline{T}}(x,y)\right]\right\}}{\sqrt{\sum_t \left[\zeta(x,y,t) - \overline{\overline{\zeta}}(x,y)\right]^2}\sqrt{\sum_t \left[T(x,y,t) - \overline{\overline{T}}(x,y)\right]^2}}. \quad (3)$$

Here $t_N = 96$, the total months of the data sets. When $\tau > 0$ ($\tau < 0$), (3) represents correlation between τ months' leading (lagging) of wind stress curl anomaly to SST anomaly.

Figure 7 shows the dependence of CCC on τ at 138°E, 43°N (in the JB) and at 130°E, 40°N (in the EKB). When

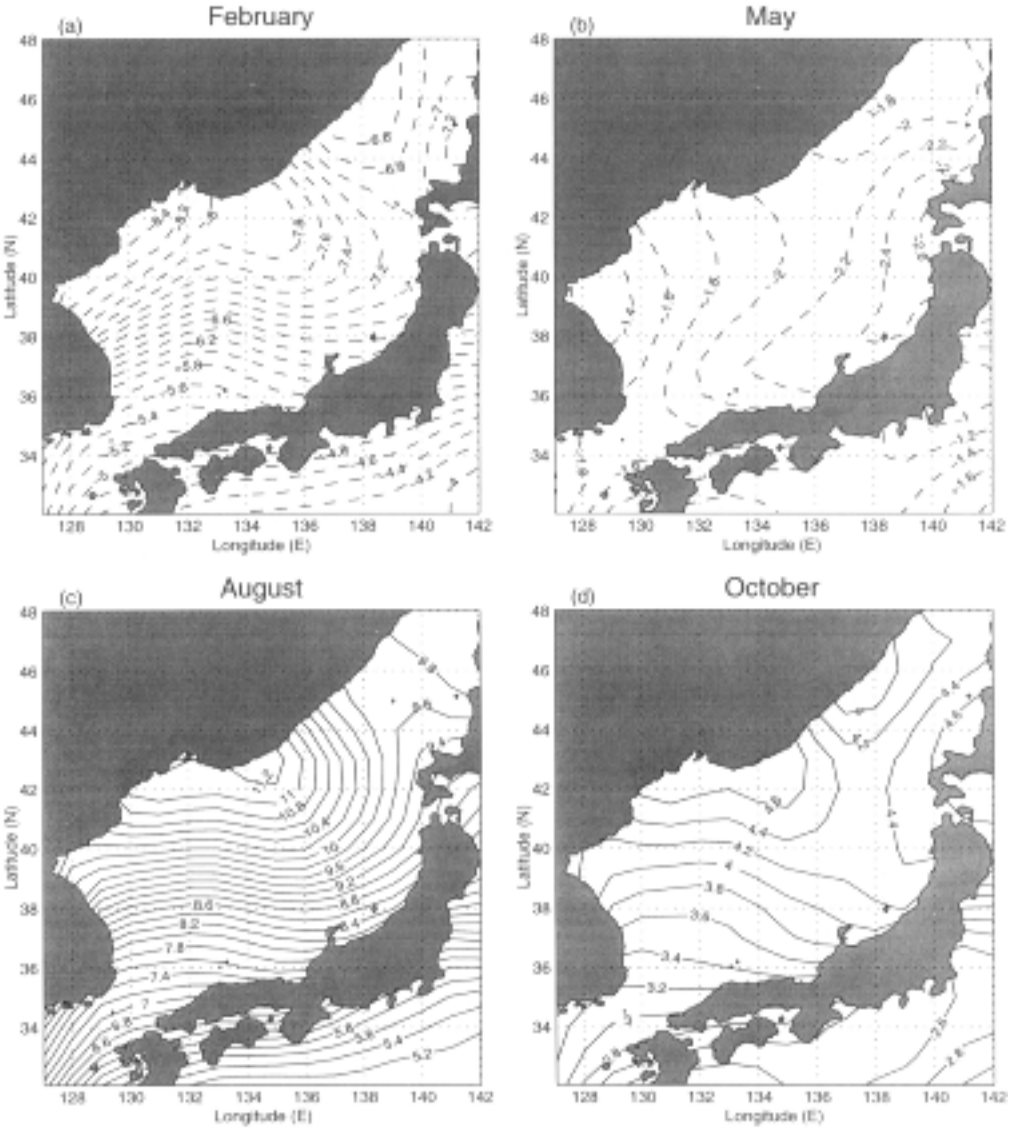

Fig. 6. Monthly SST anomalies relative to the climatological annual mean from the NCEP data set. The unit is °C.

$\tau > 0$ ($\tau < 0$), ζ leads (lags) T. We first notice that CCC is oscillatory with a strong annual signal. For the JB area, CCC has a value of –0.6 at $\tau = 0$, decreases with τ to a minimum of –0.68 at τ = one month (strongest negative correlation), and then increases with τ to near 0 at τ = 4.5 months (no correlation). CCC increases from 0 to 0.8 (maximum) as the lag τ increases from 4.5 to 7 and 8 months, and decreases again after τ = 8 months. As τ decreases from 0 to –2 (ζ lags T from 0 to 2 months), CCC increases from –0.6 to 0 (no correlation). As τ decreases from –2 to –5 (ζ lags T from 2 to 5 months), CCC increases from 0 to 0.8 (strong positive correlation). Such a pattern obviously follows from the wind stress curl variation of the monsoon nature and the seasonal change of cooling and heating conditions over the JES.

In the eastern JES near JB, the CCC is large negative (as low as –0.68) for one month leading of ζ to SST and becomes smaller (about –0.2) for one month leading of SST to ζ. In the western JES near EKB, the CCC is large positive (0.6) for one month leading of ζ to SST and becomes smaller (about 0.0) for one month leading of SST to ζ. Such an asymmetry in the CCC implies that the SST variability at the scales of the order of one month is largely due to atmospheric forcing.

4. Non-Seasonal Variation

We use the Empirical Orthogonal Function (EOF) analysis to investigate the non-seasonal variabilities of the SST, SAT, and wind stress curl fields.

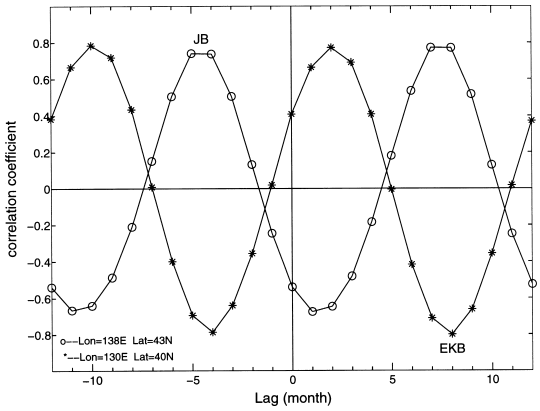

Fig. 7. Cross-correlation coefficients between the wind stress curl and SST for various lags at JB (138°E, 43°N) (circle) and EKB (130°E, 40°N) (asterisk). Here, positive (negative) lag means SST lagging (leading) the wind.

4.1 EOF analysis

The non-seasonal signals obtained by

$$\hat{\psi}\left(x_i, y_j, \tau_k, t_l\right) = \psi\left(x_i, y_j, \tau_k, t_l\right) - \overline{\psi}\left(x_i, y_j, t_l\right) \quad (4)$$

are re-arranged into a $N \times P$ matrix, $\hat{\psi}(\boldsymbol{r}_n, \tilde{t}_p)$, $n = 1, 2, ..., N$; and $p = 1, 2, ..., P$. Here $P = 156$, is the total number of time points used for computing the covariance matrix, i.e., 13 years of monthly data; $N = 272$, corresponds to the number of grids ($i = 1, 2, ..., 16$; $j = 1, 2, ..., 17$). The EOF analysis widely used in oceanographic and meteorological research (e.g., Weare *et al*., 1976; and see review by Richman, 1986; Chu *et al*. 1997a, b) is the same as Principal Component (PC) Analysis (Hotelling, 1933) in the statistics community. PCs are the amplitudes, which are functions of time, of their corresponding EOFs. These EOFs can be found by calculating the unitary eigenvectors of the covariance matrix associated with the data field. EOF analysis separates the data sets into eigenmodes. Generally speaking, each mode has an associated variance, dimensional spatial pattern, and non-dimensional time series. From this data matrix a 272-square spatial covariance matrix is calculated by

$$R = \begin{bmatrix} R_{11} & R_{12} & \cdots & R_{1N} \\ R_{21} & R_{22} & \cdots & R_{2N} \\ & \cdots & & \\ R_{N1} & R_{N2} & \cdots & R_{NN} \end{bmatrix},$$

$$R_{nm} = \sqrt{\frac{1}{P}\sum_p \hat{\psi}\left(\boldsymbol{r}_n, \tilde{t}_p\right)\hat{\psi}\left(\boldsymbol{r}_m, \tilde{t}_p\right)}, \quad N = 272, \ P = 156 \quad (5)$$

where n and m (1, 2, ..., N) denote the grid locations. The diagonal elements of the covariance matrix R_{nm} ($n = 1, 2, ..., N$) are the variance at location $\boldsymbol{r}_n$. The off-diagonal elements are the covariance with spatial lag equal to the difference between the row and column indices. This symmetric matrix has N real eigenvalues λ_α, and eigenvectors $\phi_\alpha(\boldsymbol{r}_j)$, such that

$$\sum_{j=1}^{N} R_{ij}\phi_\alpha\left(\boldsymbol{r}_j\right) = \lambda_\alpha\phi_\alpha\left(\boldsymbol{r}_i\right), \quad i = 1, 2, \ \ldots, \ N. \quad (6)$$

The eigenvectors ϕ_1, ϕ_2, ..., ϕ_N are called Empirical Orthogonal Functions. Each ϕ_α is a 272-point (16×17 grid in this study) distribution of SST anomaly pattern. The eigenvalues, λ_α ($\alpha = 1, 2, ..., N$), are all positive and the summation of them, $\sum\lambda_\alpha$, equals the total variance. Therefore, λ_α is considered as the portion of total variance "explained" by the EOF ϕ_α. It is convenient to label the eigenfunctions ϕ_α so that the eigenvalues are in descending order, i.e.,

$$\lambda_1 > \lambda_2 > \lambda_3 > \cdots: \quad (7)$$

The data matrix, $\hat{\psi}(\boldsymbol{r}_n, \tilde{t}_p)$, is thus approximately written by

$$\hat{\psi}\left(\boldsymbol{r}_n, \tilde{t}_p\right) = \sum_\alpha PC_\alpha\left(\tilde{t}_p\right)\phi_\alpha\left(\boldsymbol{r}_n\right) \quad (8)$$

where $PC_\alpha(\tilde{t}_p)$ is the principal component with a size of P, representing the temporal variation of the associated spatial pattern described by EOF $\phi_\alpha(\boldsymbol{r}_j)$.

4.2 Principal EOF modes

Spatial and temporal variabilities can be quantitatively investigated with the method of EOF analysis. In order to delineate the major SST, SAT, and ζ modes, we perform the EOF analysis and obtain the first three leading EOFs, which are able to account for 82% of the total variance of SST (Table 1), for 89.6% of the total variance of SAT (Table 2), and for 71.9% of the total variance of the surface wind stress curl (Table 3). Each EOF mode is normalized so that its total spatial variance is equal to unity. The patterns of the first three EOFs are deemed adequate to explain spatial variabilities of the JES SST (Fig. 8), SAT (Fig. 9), and wind stress curl (Fig. 10).

The first EOF mode (Fig. 8(a)) of SST accounts for 59.9% of the variance and represents the relatively homogeneous central JES and the Subpolar Front that stretches either northwestward or southwestward from the Japan coast. The central JES has warm anomaly if $PC_1 > 0$ and cold anomaly if $PC_1 < 0$. Correlation analysis shows the linkage between the first EOF mode and atmospheric warming/cooling (see Subsection 4.4). The second EOF mode of SST (Fig. 8(b)) accounts for 12.4% of the variance and shows the

Table 1. Variances of the first three leading SST EOFs.

EOF	Variance	Acumulative variance
1	0.599	0.5299
2	0.124	0.723
3	0.097	0.820

Table 2. Variances of the first three leading SAT EOFs.

EOF	Variance	Acumulative variance
1	0.692	0.692
2	0.1440	0.832
3	0.064	0.896

Table 3. Variances of the first three leading EOFs of the surface wind stress curl.

EOF	Variance	Acumulative variance
1	0.507	0.507
2	0.119	0.626
3	0.093	0.719

pattern with isolines oriented meridionally. If the density variation is assumed largely due to the temperature variability, the surface geostrophic flow almost follows the SST isolines. Thus, the second EOF mode might be associated with the Tsushima Current entering the southern Japan Sea. The third EOF mode of SST (Fig. 8(c)) accounts for 9.7% of the variance and indicates JES southern (positive) and northern (negative) opposite structure.

The first EOF mode of SAT accounts for 69.2% of the variance and represents the maximum variability near the PGB (Fig. 9(a)). The second EOF mode of SAT (Fig. 9(b)) accounts for 14.0% of the variance and shows JES southern (positive) and northern (negative) opposite structure. The third EOF mode of SAT (Fig. 9(c)) accounts for 6.4% of the variance and indicates the pattern with isolines oriented latitudinally in the northwestern half and zonally in the southeastern half. We may see the resemblance between first SAT EOF mode and first SST EOF mode, and second SAT EOF mode and third SST EOF mode.

The first EOF mode of the surface wind stress curl accounts for 22.0% of the variance and represents east-west opposite structure (Fig. 10(a)). The second EOF mode (Fig. 10(b)) accounts for 14.6% of the variance and shows the north-south opposite feature. The third EOF mode (Fig. 10(c)) accounts for 11.7% of the variance and indicates meso-scale structure at the western JES.

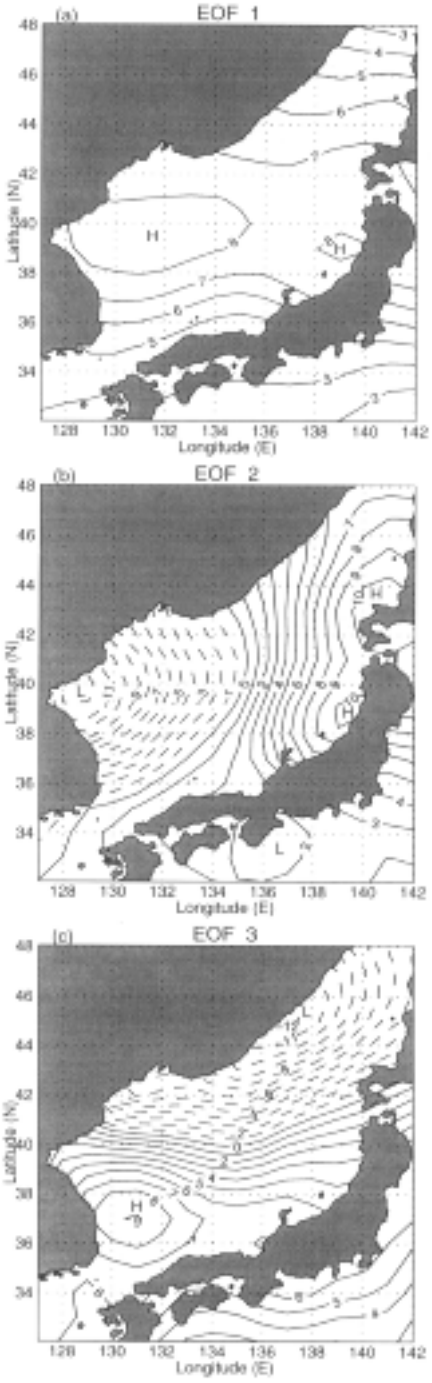

Fig. 8. The first three EOF modes of SST (unit in 0.01°C): (a) the first EOF, (b) the second EOF, and (c) the third EOF. The solid (dashed) lines indicate positive (negative) values.

4.3 Temporal variabilities of SST

The first principal component, $PC_1(\tilde{t}_p)$, for 1982–94 shows the temporal variability of the central JES warm/cold anomaly (Fig. 11). Since the first EOF mode $\phi_1(\boldsymbol{r}_n)$, is always positive throughout the whole JES (Fig. 8(a)), positive

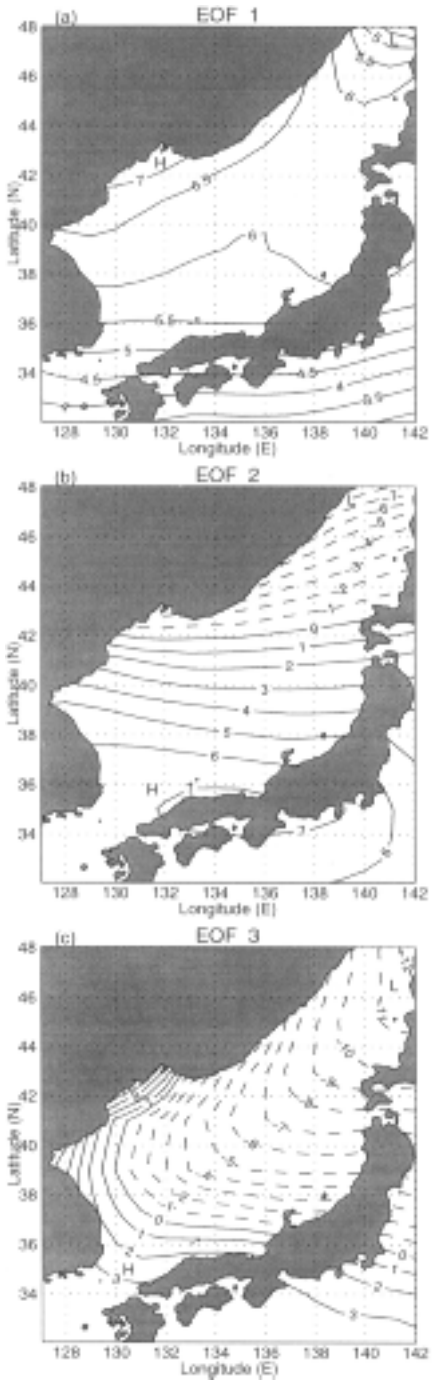

Fig. 9. Same as Fig. 8 except for SAT.

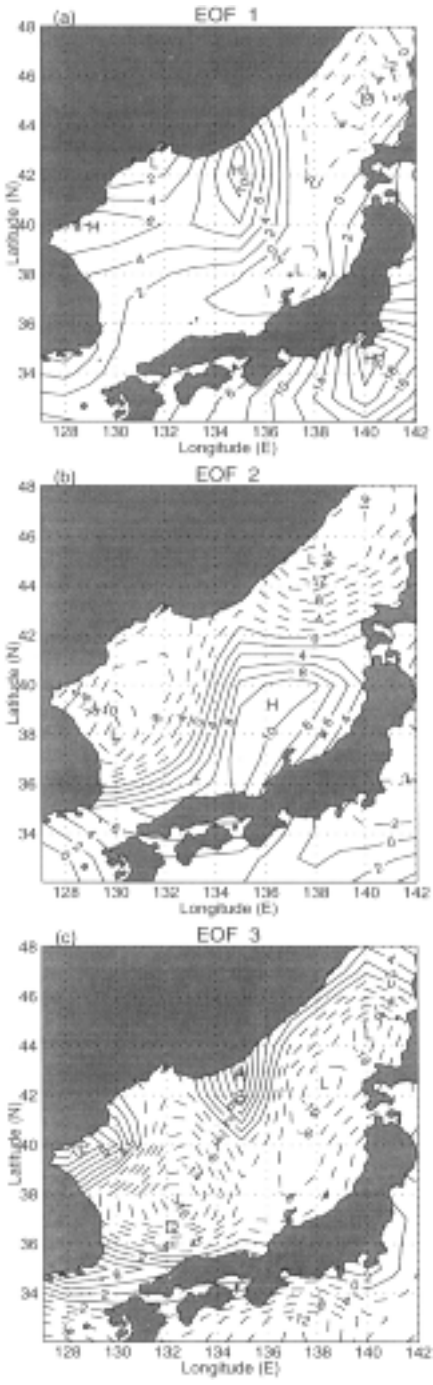

Fig. 10. Same as Fig. 8 except for surface wind stress curl (unit in 10^{-10} N/m^3).

(negative) values of $PC_1(\tilde{t}_p)$ correspond to positive (negative) SST anomalies, i.e., central JES warm (cold) anomaly. We see interannual variabilities in PC_1 over periods of 2 to 5 years (Fig. 11(a)). The maximum value of PC_1 is 32, appearing in August 1994, which indicates a strong central JES warm anomaly with monthly SST anomaly of 2.6°C [32 × (0.08°C)] in that month. The minimum value of PC_1 is –34, appearing in August 1993, which indicates a strong central JES cold anomaly with monthly SST anomaly of –2.7°C [–34 × (0.08°C)] in that month. If the isoline of 0.08°C is treated as the boundary of the central JES warm/cold anomaly (Fig. 8(a)), and if we are interested in evident warm/cool

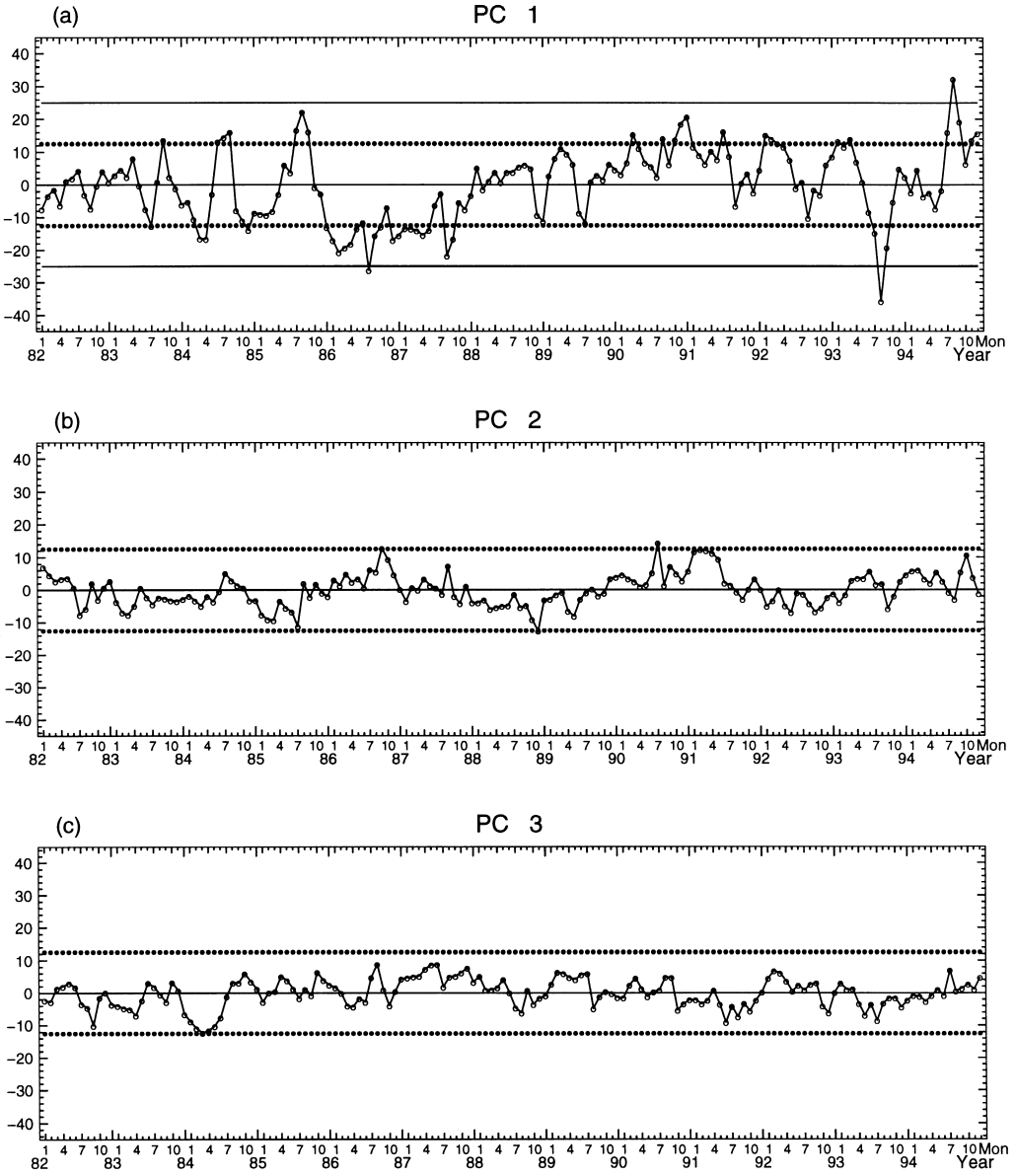

Fig. 11. Time series of the first three SST principal components for 1982–1994: (a) PC_1, (b) PC_2, and (c) PC_3. Here two solid lines are $PC_1 = \pm 25$, and two dotted lines are $PC_1 = \pm 12.5$.

anomaly occurrence with SST anomaly exceeding 2°C, we found the following criterions: When $PC_1(\tilde{t}_p) \geq 25$, the central JES has a warm anomaly with transient SST anomaly of 2°C or warmer; when $PC_1(\tilde{t}_p) \leq -25$, the central JES has a cold anomaly with transient SST anomaly of –2°C or colder. If we consider a warm (or cool) anomaly with transient SST anomaly of 1°C (or –1°C), the criterion becomes $PC_1(\tilde{t}_p) \geq 12.5$ (or $PC_1(\tilde{t}_p) \leq -12.5$). Four lines, $PC_1 = \pm 25$ (solid) and $PC_1 = \pm 12.5$ (dash), were drawn in Fig. 8 for identifying strong ($|\Delta T| \geq 2$°C) and evident ($|\Delta T| \geq 1$°C) central JES transient SST anomalies. Table 2 lists the periods of strong and evident transient SST anomalies. We found a strong warm anomaly ($\Delta T \geq 2$°C) period (August 1994), and two strong cold anomaly ($\Delta T \leq -2$°C) periods (July 1986 and August 1993). We may notice that the first EOF mode was negative in the cold seasons (November–April) of 1984–1987 and positive in the cold seasons of 1989–1993. This implies that the deep JES could be cooler in 1984–1987 because the vertical stratification is very weak in the JB in winter.

The second principal component, $PC_2(\tilde{t})$, is shown in Fig. 11(b). The difference between the maximum value of second EOF in the east JES and the minimum value in the west JES is 0.22°C. Identification of the pattern (cold west

Table 4. Central JES warm and cold anomaly periods.

	Above 2 degree C	Above 1 degree C
Warm period	Aug/94	Sep/83, Jun-Aug/84, Jul–Sep/85, Mar, Aug, Oct–Dec/90, Jun/91, Jan–Mar/92, Jan–Mar/93, Jul–Sep/94, Nov–Dec/94
Cold period	Jul/86, Aug/93	Jul/83, Mar–Apr/84, Nov/84, Dec/85–Sep/86, Nov/86–May/87, Aug–Sep/87, Jul–Sep/93

JES and warm east JES or vice versa) depends on the sign of $PC_2(\tilde{t})$. Positive (negative) $PC_2(\tilde{t})$ corresponds to the increase (decrease) of SST with longitude pattern. The maximum absolute value of PC_2 is 15, appearing in July 1990, which indicates a 3.3°C west-to-east increase of SST. The minimum value of PC_2 is –12.5, appearing in November 1988, which indicates a near 2.8°C west-to-east decrease of SST.

The third principal component, $PC_3(\tilde{t})$, is shown in Fig. 11(c). The third EOF mode represents the JES northern/southern dipole pattern. The difference between the maximum value in the southern JES and the minimum value in the ERC region is 0.2°C. Identification of the pattern (cold north JES and warm south JES or vice versa) depends on the sign of $PC_3(\tilde{t})$. Positive (negative) $PC_3(\tilde{t})$ corresponds to the decrease (increase) of SST with latitude pattern. The maximum absolute value of PC_3 is 8, appearing in August 1986, which indicates a 1.7°C south-to-north decrease of SST. The minimum value of PC_2 is –11, appearing in April 1984, which indicates a near 2.3°C south-to-north increase of SST.

4.4 CCCs among non-seasonal components

Hong *et al*. (1984) and Hirai (1994) found that winter cooling is important for the SST anomaly in the coastal area. Here, we calculated CCCs among different *PC*s of SST, SAT, and the surface wind stress curl, $C_{\mathrm{SST}_i,\mathrm{SAT}_j}(\tau)$ and $C_{\mathrm{SST}_i,\zeta_j}(\tau)$ to investigate JES air-sea interactions. The subscripts i and j mean the i-th and j-th principal components, respectively, and τ is the temporal lag. Very small values of $C_{\mathrm{SST}_i,\zeta_j}(0)$ indicate no evident relationship between non-seasonal SST and surface wind stress curl modes (Table 5). Some large values of $C_{\mathrm{SST}_i,\mathrm{SAT}_j}(0)$ denote certain connection between non-seasonal SST and SAT modes (Table 6). Comparison between Figs. 8 and 9 indicates similar spatial patterns between EOF1 of SST and EOF1 of SAT and between EOF3 of SST and EOF2 of SAT. Since we seek mechanisms causing the SST variability, the maximum positive (or minimum negative) value is picked up for each EOF mode: $C_{\mathrm{SST}_1,\mathrm{SAT}_1}(0) = 0.679$, and $C_{\mathrm{SST}_3,\mathrm{SAT}_2}(0) = 0.385$ as the most important forcing. The high correlation between SAT EOF1 and SST EOF1 indicates that the SST EOF1 pattern is caused by atmospheric warming/cooling.

Table 5. CCCs among the first three leading EOFs of SST and surface wind stress curl.

	Wind EOF1	Wind EOF2	Wind EOF3
SST EOF1	0.020	0.036	–0.062
SST EOF2	–0.039	0.027	–0.188
SST EOF3	0.010	0.097	–0.048

Table 6. CCCs among the first three leading EOFs of SST and SAT.

	SAT EOF1	SAT EOF2	SAT EOF3
SST EOF1	0.679	0.233	–0.371
SST EOF2	0.081	0.050	–0.312
SST EOF3	0.161	0.385	0.337

Figure 12 shows the dependence of $C_{\mathrm{SST}_1,\mathrm{SAT}_1}(\tau)$ and $C_{\mathrm{SST}_3,\mathrm{SAT}_2}(\tau)$ on τ. When $\tau > 0$ ($\tau < 0$), SAT leads (lags) SST. Both $C_{\mathrm{SST}_1,\mathrm{SAT}_1}(\tau)$ and $C_{\mathrm{SST}_3,\mathrm{SAT}_2}(\tau)$ are quite large at $\tau = 1$, and $C_{\mathrm{SST}_3,\mathrm{SAT}_2}(1)$ is even larger than no-lag case. On the other hand, both $C_{\mathrm{SST}_1,\mathrm{SAT}_1}(\tau)$ and $C_{\mathrm{SST}_3,\mathrm{SAT}_2}(\tau)$ are quite small at $\tau = -1$ (SST leads SAT by one month), $C_{\mathrm{SST}_1,\mathrm{SAT}_1}(-1) = 0.362$, and $C_{\mathrm{SST}_3,\mathrm{SAT}_2}(-1) = 0.110$. Such an asymmetry in the CCC implies that the SST non-seasonal variability at the scales of the order of one month is largely due to atmospheric warming/cooling.

5. Conclusions

We used the NCEP SST, SAT (1982–1994) and the NCAR surface wind stress curl (1982–1989) data to investigate the JES surface thermal variabilities and their relations to atmospheric forcing, and obtained the following results from this study.

(1) The climatological annual mean (1982–1994) SST field ($\overline{\overline{T}}$) was constructed with a modest horizontal temperature gradient, decreasing from 20°C in Tsushima Strait to 7°C in the northern JES (47°N). The climatological annual mean (1982–1989) wind stress curl field over the JES

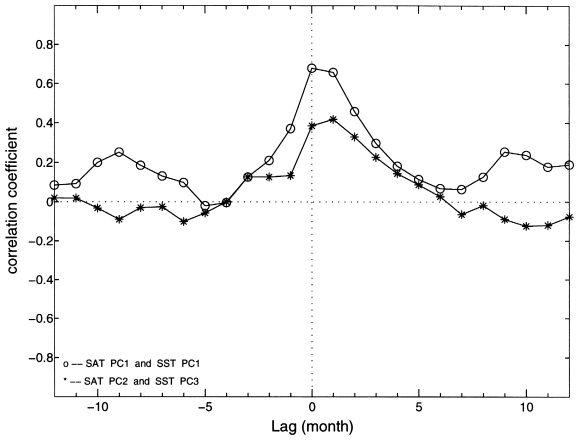

Fig. 12. Cross-correlation coefficients between non-seasonal SAT and SST modes for various lags SAT EOF1 with SST EOF1 (circle) and SAT EOF2 with SST EOF3 (asterisk).

shows a dipole pattern: cyclonic curls over the Japan Basin (JB) and anticyclonic curls over the East Korea Bay (EKB). This coincides with the prevailing northwest winds over the central JES.

(2) The seasonal variations of JES SST and surface wind stress were identified by the composite analysis. The JES SST has a cold anomaly during winter (December–February) and a warm anomaly during summer (June–September). Two locations are found to be activity centers for the four seasons: the PGB for both winter and summer, and the ERC region for the fall. The PGB has a cold center with a minimum $\tilde{T} \approx -8.4$°C in February, and has a warm center with a maximum $\tilde{T} \approx 11.2$°C in August. The surface wind stress curl anomaly has two patterns, namely, the stable (western anticyclonic and eastern cyclonic) pattern, which is strengthened in winter and weakened in summer. The annual mean field is the middle of these two levels.

(3) A strong seasonal variation with asymmetry regarding temporal lag was found in the cross-correlation coefficient between SST and surface wind stress curl: when the wind stress curl leads SST by one month the CCC is large negative (as low as –0.68) in the eastern JES and when SST leads the wind stress curl by one month the CCC becomes smaller (about –0.2). This implies that the SST variability at the scales of the order of one month is largely due to atmospheric forcing.

(4) The non-seasonal variations of JES SST, SAT, and surface wind stress curl were identified by the EOF analysis. The first EOF mode of SST accounts for 59.9% of the variance and represents a central JES warm/cold water mass. The second EOF mode of SST accounts for 12.4% of the variance and shows the pattern with isolines oriented meridionally that might be associated with the Tsushima Current entering the southern JES. The third EOF mode of SST accounts for 9.7% of the variance and indicates north-south dipole structure of the JES.

(5) In winter the JB has a weak vertical stratification. The deep water temperature is quite close to SST. The principal component of the first EOF mode of SST was negative in the cold seasons (November–April) of 1984–1987 and positive in the cold seasons of 1989–1993, implying that the deep JES could be cooler in winter of the former period (1984–1987).

(6) Cross correlation analysis on the non-seasonal components shows that there is no connection between any SST and surface wind stress curl modes and that there is a strong connection between certain SST and SAT modes: first EOF mode of SAT with first EOF mode of SST, and second EOF mode of SAT with third EOF mode of SST. The corresponding SAT and SST modes have much higher cross-correlation coefficients when the SAT mode leads the SST mode by one month than vice versa. Such an asymmetry in the CCC implies that the SST non-seasonal variability at the scales of the order of one month is largely due to atmospheric warming/cooling effect.

Acknowledgements

Surface wind stress curl data and NCEP reanalysis data were provided through NCAR and NOAA Climate Diagnostics Center, respectively. Many thanks to two anonymous reviewers and the editor (Prof. Imawaki) whose comments improved the manuscript in a great deal. This work was funded by the Office of Naval Research NOMP Program, Naval Oceanographic Office, and the Naval Postgraduate School.

References

Chu, P. C., H.-C. Tseng, C. P. Chang and J. M. Chen (1997a): South China Sea warm pool detected in spring from the Navy's master oceanographic observational data set (MOODS). *J. Geophys. Res.*, **102**(C7), 15,761–15,771.

Chu, P. C., S. H. Lu and Y. C. Chen (1997b): Temporal and spatial variabilities of the South China Sea surface temperature anomaly. *J. Geophys. Res.*, **102**(C9), 20,937–20,955.

Gong, Y. (1968): On the seasonal variation of coastal surface water temperature. *Bull. Fish. Res. Develop. Agency*, No. 3, 57–79.

Hirai, M. (1994): Evaluation of the effects of winter cooling on sea surface temperature in the spring around Tsushima Current regions. *Bull. Japan Sea Nat. Fish. Res. Ins.*, No. 44, 1–17.

Hong, C. H., K. D. Cho and S. K. Yang (1984): On the abnormal cooling phenomenon in the coastal areas of East Sea of Korea in summer 1981. *J. Oceanol. Soc. Korea*, **19**, 11–17.

Hotelling, H. (1933): Analysis of a complex of statistical variables into principal components. *J. Edu. Psych.*, **24**, 417–441, 498–520.

Isoda, Y. (1994): Interannual SST variations to the north and south of the Polar front in the Japan Sea. *La Mar*, **32**, 285–294.

Isoda, Y. and S. Saitoh (1993): The northward intruding eddy along the east coast of Korea. *J. Oceanogr.*, **49**, 443–458.

Isoda, Y., S. Saitoh and M. Mihara (1991): Sea surface tempera-

ture structure of the polar front in the Japan Sea. p. 103–112. In *Oceanography of Asian Marginal Seas*, ed. by K. Takano, Elsevier, New York.

Kano, Y. (1980): The annual variation of the temperature, salinity and oxygen contents in the Japan Sea. *The Oceanogr. Mag.*, **31**, 15–26.

Martin, S., E. Munoz and R. Drucker (1992): The effect of severe storms on the ice cover of the northern Tatarskiy Strait. *J. Geophys. Res.*, **97**(C11), 17,753–17,764.

Maizuru Mar. Observ. (1997): Climate Chart of the Japan Sea. Maizuru, Japan.

Moriyasu, S. (1972): The Tsushima current. p. 353–369. In *Kuroshio, Its Physical Aspects*, ed. by H. Stommel and K. Yoshida, University of Tokyo Press, Tokyo.

Na, J.-Y., J.-W. Seo and S.-K. Han (1992): Monthly mean sea surface wind over the adjacent seas of the Korea Peninsula. *J. Oceanol. Soc. Korea*, **27**, 1–10.

Reynolds, R. W. (1988): A real-time global sea surface temperature analysis. *J. Climate*, **1**, 75–86.

Reynolds, R. W. and D. C. Marsico (1993): An improved real-time global sea surface temperature analysis. *J. Climate*, **6**, 114–119.

Reynolds, R. W. and T. M. Smith (1994): Improved global sea surface temperature analysis using optimum interpolation. *J. Climate*, **7**, 929–948.

Richman, M. B. (1986): Rotation of principal components. *J. Climatology*, **6**, 293–235.

Seung, Y.-H. and J.-H. Yoon (1995): Some features of winter convection in the Japan Sea. *J. Oceanogr.*, **51**, 61–73.

Trenberth, K. E., J. G. Olson and W. G. Large (1989): A global ocean wind stress climatology based on ECMWF analyses. NCAR Tech. Note, NCAR/TN-338+STR, 93 pp.

Weare, B. C., A. R. Navato and R. E. Newell (1976): Empirical orthogonal analysis of Pacific sea surface temperature. *J. Phys. Oceanogr.*, **6**, 671–678.